Controlled tunnel-coupled ferromagnetic electrodes for spin injection in organic single-crystal transistors

Naber, W. J. M.; Craciun, M. F.; Lemmens, J. H. J.; Arkenbout, A. H.; Palstra, T. T. M.; Morpurgo, A. F.; van der Wiel, W. G.

Published in:
Organic Electronics

DOI:
10.1016/j.orgel.2010.01.013

Publication date:
2010

Organic Electronics 11 (2010) 743–747

Contents lists available at ScienceDirect

Organic Electronics

journal homepage: www.elsevier.com/locate/orgel

Controlled tunnel-coupled ferromagnetic electrodes for spin injection in organic single-crystal transistors

W.J.M. Naber [a,*], M.F. Craciun [a], J.H.J. Lemmens [a], A.H. Arkenbout [b], T.T.M. Palstra [b], A.F. Morpurgo [c], W.G. van der Wiel [a]

[a] NanoElectronics Group, MESA+ Institute for Nanotechnology, University of Twente, P.O. Box 217, 7500 AE Enschede, The Netherlands
[b] Solid State Chemistry Laboratory, Zernike Institute for Advanced Materials, University of Groningen, Nijenborgh 4, 9747 AG Groningen, The Netherlands
[c] DPMC and GAP, University of Geneva, 24 Quai Ernest-Ansermet, CH1211 Geneva, Switzerland

ARTICLE INFO

Article history:
Received 9 November 2009
Received in revised form 7 January 2010
Accepted 13 January 2010
Available online 22 January 2010

Keywords:
Spintronics
Organic single-crystal
Field-effect transistor
Ferromagnetic electrodes

ABSTRACT

We report on single-crystal rubrene field-effect transistors (FETs) with ferromagnetic Co electrodes, tunnel-coupled to the conduction channel via an Al_2O_3 tunnel barrier. Magnetic and electronic characterization shows that the Al_2O_3 film not only protects the Co from undesired oxidation, but also provides a highly controlled tunnel barrier for overcoming the conductivity mismatch problem when injecting spins from a ferromagnetic metal into a semiconductor. Our FETs provide a significant step towards the realization of a device that integrates FET and spin-valve functionality, one of the major goals of spintronics.

Both spin electronics (spintronics) and organic electronics have made their introduction in science and technology in the last few decades. Spintronics adds new functionality and economy to electronic devices by not only applying the electron's charge, but also its spin [1]. Organic materials particularly provide fabrication advantages, allowing for, e.g., light-weight and flexible electronics [2]. The merging of these two developments into the field of *organic spintronics* [3,4] not only potentially combines the advantages of both parental fields, but also provides additional value. Organic materials are expected to have long spin lifetimes, due to their low spin-orbit coupling and reduced hyperfine interaction, as compared to their inorganic counterparts [5]. This makes organic materials particularly interesting for application in spintronic devices.

In this article, we have made a crucial step towards the application of organic single-crystals [6] for realizing *spin-valve field-effect transistors* (*spin-valve FETs*). The long-range order of these crystals makes them the organic semiconductors with the highest carrier mobility known at the moment [7]. They are therefore a logical choice for spin-valve FETs, in which both the scattering time and spin lifetime need to be sufficiently long [3]. Recent studies on organic single-crystal FETs have shown that a broad variety of materials can be used as source and drain electrodes with good performance. Since some of those materials are ferromagnetic [8–10], the question naturally arises whether the spin polarization of the electrodes can be used to inject spins into the accumulation layer of an organic FET, to realize an electrically controlled spin-valve, i.e. a spin-valve FET [11]. This is a highly desired – but, to the best of our knowledge, yet to be realized – goal in spintronics. Unfortunately, the ferromagnetic electrode materials used so far (nickel and cobalt) are not suitable without modifications, since their oxides are antiferromagnetic and would therefore cause spin randomization during the injection of charge carriers from the metal into the organic single-crystal. Moreover, the electrodes should be tunnel-coupled to the conduction channel in the organic single-

* Corresponding author. Tel.: +31 53 489 2710; fax: +31 53 489 3343.
E-mail address: W.J.M.Naber@utwente.nl (W.J.M. Naber).

1566-1199/$ - see front matter © 2010 Elsevier B.V. All rights reserved.
doi:10.1016/j.orgel.2010.01.013

crystal, to overcome the conductivity mismatch problem of injecting spins from a metallic ferromagnet into a semiconductor [12,13].

Here we present, for the first time, FETs of 5,6,11,12-tetraphenylnaphthacene (rubrene, $C_{42}H_{28}$) single-crystals with high-quality, ferromagnetic Co electrodes and Al_2O_3 tunnel barriers, that can be used for carrier injection without spin randomization. Although the device layout, well-controlled interface, and choice of materials seem ideal for realizing the spin-valve effect, it has remained elusive in our devices so far. Possible reasons are discussed towards the end of the paper, and are expected to evoke both theoretical and experimental follow-up.

Fig. 2a is a photograph of one of our devices, showing the Co/Al_2O_3 electrodes (light bars) underneath a piece of rubrene single-crystal. Cobalt electrodes were chosen for two reasons. First, the reported workfunction of bare Co aligns favorably with the HOMO of rubrene [4], which should help in maximizing the amount of carriers injected from the electrodes into the semiconductor via tunneling (rather than thermal activation over a Schottky barrier). Second, technological processes are known, that allow the realization of a controlled and very thin Al_2O_3 layer on top of the Co film, acting at the same time as a well-defined tunnel barrier and as a protective layer against oxidation of the ferromagnet which is crucial, since CoOx is known to possess antiferromagnetic correlations, which would cause spin-flip scattering, randomizing the carrier spin during the injection. The Co electrodes (16 nm thick) are defined by photolithography on a highly doped Si/SiO_2 (300 nm) wafer and covered with a 2.5 nm Al_2O_3 tunnel barrier. The high-quality, pin-hole-free Al_2O_3 film is formed by plasma oxidation of Al evaporated on top of Co without breaking the UHV (10^{-10} Torr). This Al_2O_3 tunnel barrier prevents the Co electrodes from oxidation and helps to overcome the conductivity mismatch, as mentioned above. After lift-off with acetone, the electrodes are thoroughly cleaned in an oxygen plasma to ensure no resist is left. This is essential, as demonstrated by independent photon emission spectroscopy measurements [14]. Directly after this a rubrene single-crystal is electrostatically laminated on top of the electrodes. The lamination process yields uniform contact without air gaps, bubbles or interference fringes [6]. Similar single-crystal FET geometries were studied before in the case of non-ferromagnetic electrodes [6,8,9].

In order to verify the critical features of our device, we first performed the experiments described below. A Co/Al_2O_3/NiFe(permalloy) magnetic tunnel junction (MTJ [15], see inset of Fig. 1a) was used to check the quality of the Co/Al_2O_3 electrodes after exposure to air, acetone and oxygen plasma cleaning. To mimic the FET device fabrication process, the calibrated 2.0 nm thick Al film (resulting in a 2.5 nm thick layer of Al_2O_3) on top of the Co film (both grown in UHV) is first plasma oxidized for 10 min, exposed to air, covered with photoresist, cleaned by acetone and isopropanol, and oxidized again for 10 min to remove photoresist remnants and clean the bottom electrode. The MTJ is completed by evaporating the NiFe top electrode in UHV again. The magnetoresistance of a representative MTJ thus fabricated, is shown in Fig. 1a. We observe a clear hysteresis and a magnetoresistance (*MR*) of 16%, very close to the value of clean interfaces produced without breaking the vacuum (also shown in Fig. 1a), implying the good quality of the Al_2O_3 tunnel barrier (protecting the underlying Co from oxidation) and its robustness under our FET fabrication process. The realization of air-exposed FM electrodes in an organic spin-valve structure has been demonstrated before [16], but here an additional (and essential) cleaning step is used to remove any organic contaminations.

For spin valves, the ability to reverse the magnetization of the injector and detector electrodes independently is essential [1]. Therefore, the switching fields of both electrodes need to be sufficiently different. The magnetization of the 16 nm Co layer is in plane, and its switching field depends on the ratio between length and width. The switching fields H_{sw} of the Co/Al_2O_3 electrodes for different electrode widths d were determined from test samples with an ensemble of electrodes (see right inset of Fig. 1b), using the same fabrication procedure and substrate as for the FET devices. Hysteresis curves measured in a vibrating sample magnetometer (VSM) clearly reveal sharp switching fields, as shown in the left inset of Fig. 1b for the case of a test sample containing an ensemble

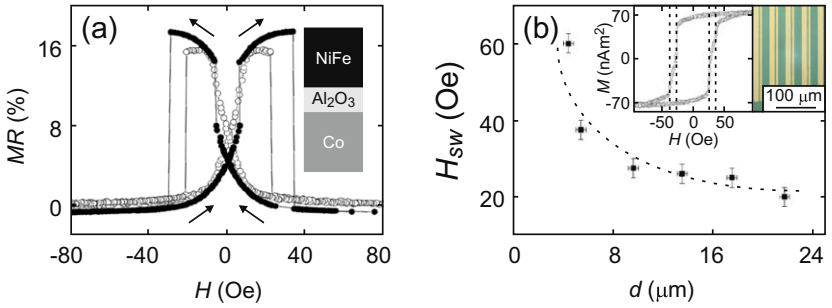

Fig. 1. Electrode characterization. (a) Magnetoresistance *MR* vs. magnetic field *H* for Co/Al_2O_3(~2.5 nm)/NiFe(15 nm) magnetic tunnel junctions (MTJs, inset). Data shown for a MTJ with 16 nm Co layer treated with photoresist, acetone and IPA (open circles) and an untreated one with a 8 nm Co layer (solid dots). *MR* is defined as $(R - R_P)/R_P$, with R_P the resistance for parallel magnetization of the Co and NiFe layers at large magnetic fields. Arrows denote the sweep directions. Different switching fields due to difference in Co layer thickness. (b) Switching field H_{sw} vs. electrode width d for Co/Al_2O_3 (16 nm/2.5 nm) electrodes. The dotted line is a guide to the eye. Left inset: Magnetization *M* vs. magnetic field *H* for electrodes with a width of 5.4 and 13.5 ± 0.4 μm. The switching field H_{sw} for the two widths is denoted by the dashed lines. Right inset: Ensemble of electrodes for H_{sw} measurements.

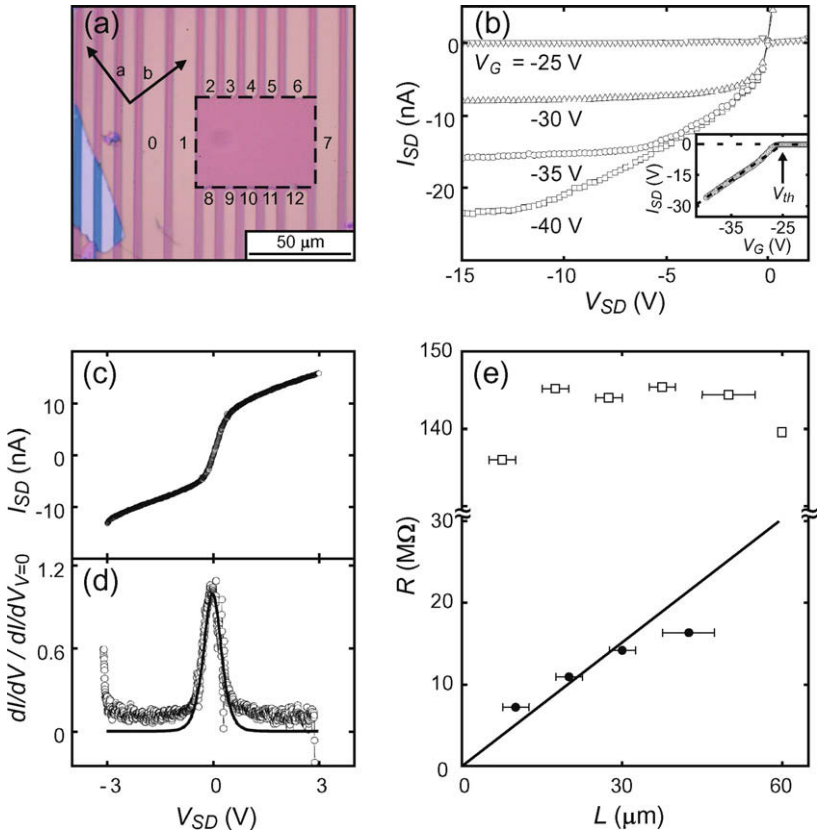

Fig. 2. Single-crystal FET device. (a) Photograph of the rubrene single-crystal (partly) overlapping with Co/Al_2O_3 electrodes (numbered 0–12; other electrodes not used). Electrodes 1, 6, 7 and 12 have 12 ± 0.4 μm width, 2–5 and 8–11, 6.5 ± 0.4 μm. The doped Si substrate is used as back gate. The active device area is denoted by the dashed rectangle, with channel length $L = 60$ μm and width $W = 50$ μm. The crystal axes *a* and *b* (the latter corresponding to the highest mobility) are denoted by the arrows. (b) Source–drain current I_{SD} vs. voltage V_{SD}(electrodes 1 and 7) for different gate voltages V_G. Inset: I_{SD} vs. V_G for $V_{SD} = -10$ V. The threshold voltage $V_{th} = -25$ V is indicated by the arrow. (c) Zoom-in around $V_{SD} = 0$ V($V_G = -40$ V) for the measurements in (b). (d) Normalized differential conductance $dI/dV / dI/dV_{V=0}$ vs. V_{SD}. The line is a fit to the derivative of Eq. (1). (e) Resistance *R* vs. channel length *L* for two-terminal measurements (open squares) for $V_{SD} = -1$ V and 4-terminal measurements (solid dots) for $I_{SD} = -1$ nA (linear regime, $V_G = -40$ V for all measurements). The solid line is a fit to Eq. (3).

of electrodes with two different widths (5.4 and 13.5 ± 0.4 μm). From these VSM measurements the switching field as a function of electrode width is derived, see Fig. 1b. H_{sw} strongly depends on electrode width for $d < 10$ μm, but saturates for wider electrodes.

The multi-terminal single-crystal device of Fig. 2a is characterized using different measurement configurations, and the main characteristics have been reproduced in multiple devices. The negative Si back gate voltage (used to induce holes) is expected to be screened by the Co/Al_2O_3 electrodes, i.e. the charge accumulation should be much lesser on top of the electrodes than at the crystal/SiO_2 interface in between the electrodes. To confirm this, a voltage of −10 V was applied between electrode 0 and 7 for a gate voltage of −40 V. No current larger than 10^{-11} A was measured. We conclude that, although current between adjacent electrodes can flow over the full crystal width, for non-adjacent electrodes there is only a current path through the non-contacted region (channel width $W = 50$ μm, channel length $L = 60$ μm) denoted by the dashed lines in Fig. 2a. Using electrodes 1–12, 2- and 4-terminal measurements are performed. The multi-terminal layout is also suitable for measuring spin accumulation in the so-called non-local geometry [17].

For 2-terminal measurements, the source–drain voltage V_{SD} is applied over electrodes 1 and 7, and the resulting current I_{SD} is measured using the same electrodes. Different contact combinations are discussed later on. I_{SD}–V_{SD} curves for different gate voltages V_G are shown in Fig. 2b. The typical gate leakage current in our devices is $I_{leak} < 10^{-11}$ A. The threshold voltage V_{th} is −25 V (inset of Fig. 2b), obtained from extrapolating the I_{SD}–V_G curves for large V_G (linear regime) to $I_{SD} = 0$. This value is relatively high, and might be related to hole trapping at the SiO_2/single-crystal interface or incomplete lamination of the crystal to the substrate.

The weak gate dependence around $V_{SD} = 0$ V implies that the device resistance is contact-dominated [8,9], as discussed in more detail below. The contact-dominated behavior is expected, since we have a tunnel barrier on top of the Co electrodes. The reasonable contact quality without a large hole injection barrier is demonstrated by

the linearity at $V_{SD} = 0$ V, as can be seen in Fig. 2c [18]. The overall non-linear shape around $V_{SD} = 0$ (see Fig. 2c) can be described by a back-to-back diode model [8]

$$I_{b-b} = I_0 \tanh\left(\frac{eV_{SD}}{2\eta k_B T}\right), \quad (1)$$

where I_0 is the saturation current, η the diode ideality factor, k_B the Boltzmann constant and T the temperature. The normalized differential conductance, obtained by numerical differentiation of the data, can be fitted by the derivative of Eq. (1), as shown in Fig. 2d. The small offset is explained by the fact that I_0 is weakly bias dependent, contrary to what is assumed in the derivation of Eq. (1). We obtain a value $\eta = 7.7 \pm 0.2$, as compared to $\eta = 1$ for an ideal Schottky diode. This high value demonstrates that although Schottky barrier formation plays a role in our devices, tunneling is important [19] and holes are indeed injected in the single-crystal through the tunnel barrier. Temperature-dependent measurements should give more insight into the height of the Schottky barriers.

In the linear regime, the usual FET relation applies

$$I_{SD} = \frac{W}{L}\mu C_i (V_G - V_{th}) V'_{SD}, \quad (2)$$

where C_i the capacitance of the gate insulator per unit area and μ the carrier mobility. Note that V'_{SD} is the voltage drop over the conducting channel, excluding the voltage drop over the electrodes. The channel resistance R_{ch} is determined from 4-terminal measurements. Current is driven between electrodes 1 and 7, the voltage drop is measured using the intermediate electrodes, to study the channel resistance as a function of length, see Fig. 2e (solid dots). Note that the square resistance $R_\square \sim 25\ \mathrm{M\Omega/\square}$ is $\sim 10^3$ times the quantum resistance. By rewriting Eq. (2), R_{ch} is given by

$$R_{ch} = \frac{L}{WC_i(V_G - V_{th})}\frac{1}{\mu}. \quad (3)$$

Fitting to Eq. (3), we extract a hole mobility of $0.25\ \mathrm{cm^2(Vs)^{-1}}$. The relatively low mobility is attributed to contaminations in the starting material (only one purification cycle is used) and the rather long period (∼weeks) between crystal growth and device fabrication. Although the crystals are stored in a nitrogen environment, oxidation cannot completely be ruled out [20]. Optimization of these factors has proven to result in typically 1–10 $\mathrm{cm^2\,(Vs)^{-1}}$ mobilities [21].

The 2- and 4-terminal resistance measurements are compared in Fig. 2e, where the difference is explained by the contact resistance. The normalized contact resistance R_cW of $0.28\ \mathrm{M\Omega\,cm}$ (used in 2D devices) dominates the 2-terminal resistance, as concluded before. This is much higher than contact resistances found for nickel oxide electrodes ($0.1 - 1\ \mathrm{k\Omega\,cm}$) [10] and cobalt oxide electrodes (10–200 $\mathrm{k\Omega\,cm}$) [8]. The high contact resistance in our devices can be explained by the Al_2O_3 tunnel barrier, and implies that charge is injected through the tunnel barrier, as intended.

In spite of the seemingly ideal choices for the spin injecting and detecting interfaces, we have not been able to unambiguously demonstrate a spin-valve effect in our FETs. This could have several reasons. First of all, the spin relaxation time τ_{sf} may be not as long as expected. Based on EPR studies [22], we have assumed a lower bound of 1 μs for τ_{sf}. Using $\lambda_{sf} = \sqrt{D\tau_{sf}}$, where λ_{sf} is the spin relaxation length, D the diffusion constant, and the Einstein relation $D = \mu k_B T/e$, gives $\lambda_{sf} > 1\ \mu\mathrm{m}$, comparable to the present device dimensions. Recently, even much larger values (∼ mm) were predicted for rubrene single-crystals [23]. However, if τ_{sf} is significantly shorter, we should make the channels shorter and/or use crystals with higher mobility. We cannot exclude that τ_{sf} is temperature dependent as well and is longer at lower temperatures. Devices similar to those demonstrated here, with shorter channel length, will provide a well-controlled experimental platform to investigate the conditions for the occurrence of spin injection in organic semiconductors.

In conclusion, we have succeeded to realize well-defined tunnel barriers between ferromagnetic electrodes and organic single-crystals. The high-quality tunnel barrier should allow for spin injection without randomization. This, in combination with the observed FET functionality, provides us with necessary conditions for demonstrating a spin-valve FET. Similar devices are also expected to shine light on the spin relaxation time in organic semiconductors and the underlying physical mechanisms.

Acknowledgements

We thank J.G.M. Sanderink, A.S. Molinari, B.C. Min, R. Jansen, S.P. Dash, T. Banerjee and D.N. Reinhoudt for fruitful discussions and help. This work is part of WGvdW's VIDI research program 'Organic materials for spintronic devices', financially supported by the Netherlands Organization for Scientific Research (NWO) and the Technology Foundation STW.

References

[1] G.A. Prinz, Physics Today 48 (1995) 58;
G.A. Prinz, Science 282 (1998) 1660;
S.A. Wolf et al., Science 294 (2001) 1488.
[2] R. Farchioni, G. Grosso, Organic Electronic Materials, Springer-Verlag, Berlin, 2001;
G. Cuniberti, G. Fagas, K. Richter (Eds.), Introducing Molecular Electronics, Springer-Verlag, Berlin, Heidelberg, 2005;
H. Klauk (Ed.), Organic Electronics: Materials, Manufacturing and Applications, Wiley-VCH, Weinheim, 2006.
[3] W.J.M. Naber, S. Faez, W.G. van der Wiel, J. Phys. D: Appl. Phys. 40 (2007) R205.
[4] V.A. Dediu, L.E. Hueso, I. Bergenti, C. Taliani, Nature Mat. 8 (2009) 707.
[5] S. Sanvito, A.R. Rocha, J. Comput. Theor. Nanosci. 3 (2006) 624.
[6] R.W.I. de Boer, M.E. Gershenson, A.F. Morpurgo, V. Podzorov, Phys. Stat. Sol. (a) 201 (2004) 1302.
[7] V. Podzorov, E. Menard, A. Borissov, V. Kiryukhin, J.A. Rogers, M.E. Gershenson, Phys. Rev. Lett. 93 (2004) 086602.
[8] A.S. Molinari, I. Gutiérrez, I.N. Hulea, S. Russo, A.F. Morpurgo, Appl. Phys. Lett. 90 (2007) 212103.
[9] A.S. Molinari, G. Lezama, P. Parisse, T. Takenobu, A.F. Morpurgo, Appl. Phys. Lett. 92 (2008) 133303.
[10] I.N. Hulea, S. Russo, A. Molinari, A.F. Morpurgo, Appl. Phys. Lett. 88 (2006) 113512.
[11] C.L. Dennis, C.V. Tiusan, J.F. Gregg, G.J. Ensell, S.M. Thompson, IEE Proc.–Circuits Devices Syst. 152 (2005) 340;
S. Sugahara, IEE Proc.–Circuits Devices Syst. 152 (2005) 355.
[12] G. Schmidt, D. Ferrand, L.W. Molenkamp, A.T. Filip, B.J. van Wees, Phys. Rev. B 62 (2000) R4790.
[13] A. Fert, H. Jaffrès, Phys. Rev. B 64 (2002) 184420.

[14] M. Grobosch, C. Schmidt, W.J.M. Naber, W.G. van der Wiel, M. Knupfer, Synthetic Metals, in press, 2009, doi:10.1016/j.synthmet.2009.09.014.
[15] J.S. Moodera, L.R. Kinder, T.M. Wong, R. Meservey, Phys. Rev. Lett. 74 (1995) 3273.
[16] G. Szulczewski, H. Tokuc, K. Oguz, J.M.D. Coey, Appl. Phys. Lett. 95 (2009) 202506.
[17] M. Johnson, R.H. Silsbee, Phys. Rev. Lett. 55 (1985) 1790.
[18] N. Kawasaki, Y. Ohta, Y. Kubozono, Appl. Phys. Lett. 91 (2007) 123518.
[19] S.M. Sze, K.K. Ng, Physics of Semiconductor Devices, Wiley, New Jersey, 2007.
[20] C. Kloc, K.J. Tan, M.L. Toh, K.K. Zhang, Y.P. Xu, Appl. Phys. A 95 (2009) 219.
[21] A.F. Stassen, R.W.I. de Boer, N.N. Iosad, A.F. Morpurgo, Appl. Phys. Lett. 85 (2004) 3899;
I.N. Hulea, S. Fratini, H. Xie, C.L. Mulder, N.N. Iossad, G. Rastelli, S. Ciuchi, A.F. Morpurgo, Nat. Mat. 5 (2006) 982.
[22] V.I. Krinichnyi, Synth. Met. 108 (2000) 173.
[23] J.H. Shim, K.V. Raman, Y.J. Park, T.S. Santos, G.X. Miao, B. Satpati, J.S. Moodera, Phys. Rev. Lett. 100 (2008) 226603.